

OPTIMAL CONTROL OF THIN-FILM FLOW ON A FLEXIBLE TOPOGRAPHY

S. ALRASHIDY*, A. KALOGIROU†, D. KALISE‡, AND K. G. VAN DER ZEE§

Abstract. This work presents a mathematical model for the optimal control of thin-film flows over a flexible topography influenced by an external force. Our thin-film model allows for the rupture of films as well as the coalescence of bubbles. The objective is to find the optimal distributed force acting on the topography that minimises the differences between actual and desired thin-film profiles. A nonlinear lubrication equation governing the fluid dynamics and appropriate functional settings for this model are presented. It is also shown that this system satisfies a global energy-dissipation law for a suitable energy functional. Optimality conditions are derived for the solution of the minimisation problem of a specified cost function across a time horizon. These conditions are formulated at a continuous level as system of coupled, forward-backward PDEs, which are subsequently discretised for numerical investigation. To ensure computational efficiency and stability, first-order Implicit-Explicit (IMEX) time-stepping schemes are employed to handle the nonlinearities in the model, and a reduced gradient descent algorithm is applied to obtain a numerical approximation of the optimal control signal. Numerical results illustrate that controlling the thin film, even during rupture, achieves a precise film profile. This control strategy accelerates convergence towards a steady state, reduces instabilities, stabilises dewetting processes, and meets the desired profile specifications.

Key words. thin-film flows, optimal control of fluid flow, reduced gradient, IMEX methods.

AMS subject classifications. 35Q93, 76A20, 49K20, 49M41

1. Introduction. Controlling thin-film flow has gained significant interest across a range of applications [15, 28, 38, 44, 51]. For example, coating processes favour stable, flat-flow films [48], whereas applications in heat and mass transfer often require interfacial deformations [16]. Motivation stems from the increasing number of thin-film devices manufactured across diverse industries such as microelectronics, displays, optical storage, and microfluidic devices [15, 28, 38, 43, 44]. These applications all require a thorough understanding and control of the thin layer deposition process and the free surface profile [13, 43]. However, efficient control of interfacial shape or surface area has been largely unexplored until recently, with most efforts focusing on varying external mechanisms like electric fields [3, 50], including a rigid topography [18, 19, 41, 42, 49] or surfactants [9], rather than using mathematically optimal or robust approaches [51].

The mathematical model of thin films is based on the lubrication approximation simplified from the Navier-Stokes equations [40], resulting in a time-dependent Partial Differential Equation (PDE) for the height of the film. This model has been extensively studied for its ability to facilitate accurate analytical and numerical calculations [2, 30, 34, 35]. This indicates that the characteristic wavelengths of interfacial deformation are significantly larger than the film thickness ratio [39, 48]. Additionally, when combined with flexible topographies, further dynamics arise due to elasto-hydrodynamics [34, 35]. Craster and Matar’s review provides a comprehensive overview of

*School of Mathematical Sciences, University of Nottingham, University Park, Nottingham NG7 2RD, UK (sattam.alrashidy@nottingham.ac.uk). Department of Mathematics, Islamic University of Madinah, Madinah, Saudi Arabia (sattamjr@iu.edu.sa).

†School of Mathematical Sciences, University of Nottingham, University Park, Nottingham NG7 2RD, UK (anna.kalogirou@nottingham.ac.uk).

‡Department of Mathematics, Imperial College London, London SW7 2AZ, UK (d.kalise-balza@imperial.ac.uk).

§School of Mathematical Sciences, University of Nottingham, University Park, Nottingham NG7 2RD, UK (kg.vanderzee@nottingham.ac.uk).[¶]

these models [11]. Traditional models typically assume rigid substrates, but real-world applications increasingly involve flexible topographies [35].

Our work develops a PDE-constrained optimisation approach for the control of thin-film flows over a flexible topography. Our thin film model allows for the rupture of films as well as the coalescence of bubbles. We focus on finding the distributed force influencing the flexible topography that minimises a cost function, for example, the difference between the observed height of the thin film and some desired function.

Novelty and contributions. The main contributions of our work are as follows:

1. We first present an appropriate functional setting for the PDE system consisting of a thin-film equation coupled to a flexible substrate equation. We show that this system satisfies a global energy-dissipation law for a suitable energy functional. Next, we derive the optimality conditions at the continuous level. To achieve this, we formulate an optimal control problem consisting of the minimisation of a cost functional subject to the nonlinear evolution PDE for the thin-film flow controlled by the bottom topography. First-order optimality conditions are given by forward-backward, state-adjoint PDE system, closed with an optimality condition for the control.
2. Our second main contribution is that we propose a stable time discretisation for the optimality system. In particular, a careful treatment of the nonlinearity in the model (i.e., the disjoining-pressure term) is needed to balance computational efficiency and stability. For this, we explore first-order Implicit-Explicit (IMEX) time-stepping schemes, which decompose the nonlinear term into a contractive (convex) and expansive (concave) component [37, 52]. This scheme can be combined with any spatial discretisation method. We have employed standard continuous finite elements. Finally, gradient descent is used as an iterative method to solve the resulting discrete PDE-constrained optimisation problem [12, 33].

The structure of the rest of the paper is as follows. Section 2 introduces the model for the flow of thin films over a flexible topography and its weak form. Section 3 shows the optimal control problem, the first-order necessary optimality conditions, and the gradient descent scheme for the optimisation problem. Section 4 presents the time discretisation using the IMEX time-stepping schemes and the numerical results. Finally, Section 5 summarises the findings of this work.

2. Model of thin-film flow over a flexible topography. In this section, we present a mathematical model comprising two coupled PDEs that describe the evolution of the thin film and flexible substrate. Furthermore, we show the model's functional settings and weak form. The derivation of thin-film flow models on rigid substrates is well known and is based on lubrication theory [5, 49]. The inclusion of the disjoining pressure and a non-inclined flexible substrate is discussed in various forms in the literature [2, 11, 30, 34, 35, 36].

2.1. State equation. We consider a two-dimensional thin-film flowing on the underside of a flexible substrate; an abstract sketch of this setup is illustrated in Figure 1. The coordinate system is defined by (x, y) , with x being the horizontal coordinate and y being the vertical coordinate. We also define t as time. The force driving the flow is gravity g , which, contrary to the usual direction, is oriented upwards to model the scenario where the fluid flows beneath a substrate.

The following system governs the evolution of a thin film over a flexible topogra-

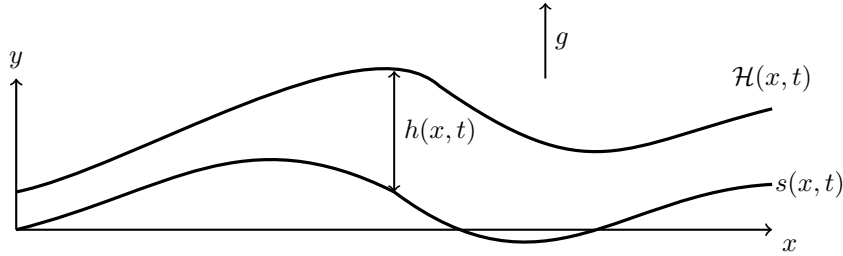


Fig. 1: Illustration of a two-dimensional fluid flow over topography. $h(x, t)$ denotes the film thickness, $s(x, t)$ the topography, and $\mathcal{H}(x, t) = h(x, t) + s(x, t)$ the height of the free surface. The gravity vector g points upwards to indicate flow under a wall.

phy, i.e.,

$$(2.1) \quad \mathcal{H}(x, t) := h(x, t) + s(x, t),$$

where $\mathcal{H}(x, t)$ is the observed film height relative to flat horizontal reference, $h(x, t)$ is the film thickness, and $s(x, t)$ is the substrate topography height:

$$(2.2a) \quad h_t - \left(\frac{1}{3}h^3\mu_x\right)_x = 0,$$

$$(2.2b) \quad \mu = \phi'(h) - \frac{B_o}{C_a}\mathcal{H} - \frac{1}{C_a}\mathcal{H}_{xx},$$

$$(2.2c) \quad s_t - c^2s_{xx} - \frac{\gamma}{C_a}(h_{xx} + B_o h) = f(x, t).$$

In (2.2a), we introduced μ to reduce the fourth-order thin film PDE to a coupled system of second-order equations¹. In (2.2b), the disjoining pressure $\Pi(h) = -\phi'(h)$ is included to model film rupture, where $\phi(h)$ represents the interface potential capturing molecular interactions between liquid molecules and air [14] (see Section 2.3 for examples of $\phi(h)$). Here, C_a and B_o denote the capillary and Bond numbers, respectively². Equation (2.2c) represents a one-dimensional force balance on the topography, considering both the topography's damping and its elastic characteristics, where f represents an external force that influences the topography. The parameters c and γ are dimensionless measures of the topography tension and film damping, respectively [2].

The system is solved over a time interval $t \in [0, T]$, where T is the final time, and in a finite domain of arbitrary length L , i.e. $x \in \Omega := [0, L]$. The initial conditions

¹Furthermore, when integrating μ using the finite element method, we find that the highest derivative is of the first order when we apply test functions.

²The capillary and Bond numbers are dimensionless parameters common in fluid dynamics problems. They represent the importance of viscous forces or gravitational forces compared to surface tension forces on a fluid's surface, respectively. They are defined as

$$C_a = \frac{\bar{\mu}U}{\sigma}, \quad B_o = \frac{\rho gh_0^2}{\sigma},$$

where $\bar{\mu}$ and ρ are the fluid's viscosity and density, respectively, U is a typical velocity, σ is the surface tension, h_0 is a typical length scale, and g is gravity. See [27] for typical values these parameters can take in real-life scenarios

are specified by setting

$$(2.3) \quad h(x, 0) = h_0(x), \quad s(x, 0) = s_0(x).$$

Furthermore, homogeneous Neumann boundary conditions are applied at the domain boundaries

$$(2.4) \quad h_x = \mu_x = s_x = 0, \quad \text{at } x = 0 \text{ and } x = L.$$

We now clarify the free-energy dissipation in our model (2.2). Understanding the energy dissipation mechanisms is important for ensuring the stability and physical relevance of the model. We begin by defining the total free-energy functional:

$$(2.5) \quad \mathcal{E}(h, s) = \int_{\Omega} \left[\phi(h) - \frac{B_0}{2C_a} h^2 + \frac{1}{2C_a} h_x^2 + \frac{c^2}{2\gamma} s_x^2 + \frac{1}{C_a} (h_x s_x - B_o h s) \right] dx,$$

which consists of the molecular free energy $\phi(h) - \frac{B_o}{2C_a} h^2$, surface free energy $\frac{1}{2C_a} h_x^2$, elastic free energy $\frac{c^2}{2\gamma} s_x^2$, and fluid–substrate interaction energy $\frac{1}{C_a} (h_x s_x - B_o h s)$. This free energy functional satisfies the following law (the full derivation is shown in Appendix A):

$$(2.6) \quad \underbrace{\frac{d}{dt} \mathcal{E}(h, s)}_{\text{Change in energy}} = - \underbrace{\left(\frac{1}{3} \int_{\Omega} h^3 \mu_x^2 dx + \frac{1}{\gamma} \int_{\Omega} s_t^2 dx \right)}_{\text{Dissipation}} + \underbrace{\frac{1}{\gamma} \int_{\Omega} f s_t dx}_{\text{External work}},$$

where the terms on the right-hand side of (2.6) are the dissipation in the fluid and substrate, and the work done by the external force on the substrate. Note that bracket in the dissipation term is non-negative (since $h \geq 0$), hence, in the absence of external work, the total free energy is non-increasing in time.

It is well known that a free-energy dissipation law such as (2.6) is critical in the study of well-posedness of thin-film flow models, see for example, [6, 7, 8, 20, 29]. The well-posedness of system (2.2) is outside of the scope of this work. We believe such a study could be applied to the natural weak formulation of the problem, which we present next.

2.2. Weak form of the state equations. We consider a mixed weak formulation of the state system (2.2), wherein h , μ , and s are considered as independent variables. We introduce Hilbert spaces \mathcal{L} and \mathcal{V} of functions dependent on time $t \in (0, T)$, possessing values in $L^2(\Omega)$ and $H^1(\Omega)$, respectively, and their norms:

$$(2.7a) \quad \mathcal{L} := L^2(0, T; L^2(\Omega)), \quad \|v\|_{\mathcal{L}}^2 := \int_0^T \|v(t)\|_{L^2(\Omega)}^2 dt,$$

$$(2.7b) \quad \mathcal{V} := L^2(0, T; H^1(\Omega)), \quad \|v\|_{\mathcal{V}}^2 := \int_0^T \|v(t)\|_{H^1(\Omega)}^2 dt.$$

The spaces \mathcal{L} and \mathcal{V} are fit for f and μ , respectively. A suitable space \mathcal{W} for h and s is defined by:

$$(2.8) \quad \mathcal{W} := \{v \in \mathcal{V} : v_t \in \mathcal{V}^* := L^2(0, T; H^1(\Omega)^*)\},$$

where $H^1(\Omega)^*$ is the dual space of $H^1(\Omega)$, that is, the space of all continuous linear functionals on $H^1(\Omega)$. In addition, to strongly impose the initial conditions (2.3) for h and s , we establish

$$(2.9) \quad \mathcal{W}_{v_0} := \{v \in \mathcal{W} : v(0) = v_0\},$$

for any $v_0 \in \mathcal{L}$.

The weak formulation of (2.2) reads as follows (recall $\mathcal{H} = h + s$):

Find $(h, \mu, s) \in \mathcal{W}_{h_0} \times \mathcal{V} \times \mathcal{W}_{s_0}$, such that for $t \in (0, T]$,

$$(2.10a) \quad \langle h_t, v \rangle + \frac{1}{3} (h^3 \mu_x, v_x) = 0, \quad \forall v \in H^1(\Omega),$$

$$(2.10b) \quad (\mu, w) - (\phi'(h), w) + \frac{B_o}{C_a} (\mathcal{H}, w) - \frac{1}{C_a} (\mathcal{H}_x, w_x) = 0, \quad \forall w \in H^1(\Omega),$$

$$(2.10c) \quad \langle s_t, \psi \rangle + c^2 (s_x, \psi_x) + \frac{\gamma}{C_a} ((h_x, \psi_x) - (B_o h, \psi)) = (f, \psi), \quad \forall \psi \in H^1(\Omega),$$

where $\langle \cdot, \cdot \rangle$ signifies the duality pairing between $H^1(\Omega)^*$ and $H^1(\Omega)$, and (\cdot, \cdot) is the inner product in $L^2(\Omega)$.

The system (2.10) can also be written as an aggregated space–time weak formulation:

Find $(h, \mu, s) \in \mathcal{W}_{h_0} \times \mathcal{V} \times \mathcal{W}_{s_0}$:

$$(2.11a) \quad \int_0^T \left(\langle h_t, v \rangle + \langle s_t, \psi \rangle - (\phi'(h), w) + \left(\frac{1}{3} h^3 \mu_x, v_x \right) \right) dt \\ + \mathcal{A}((h, s, \mu), (v, w, \psi)) = \int_0^T (f, \psi) dt, \quad \forall (v, w, \psi) \in \mathcal{V} \times \mathcal{V} \times \mathcal{V},$$

where the bilinear form \mathcal{A} takes all linear terms:

$$(2.11b) \quad \mathcal{A}((h, s, \mu), (v, w, \psi)) := \int_0^T \left((\mu, w) + \frac{B_o}{C_a} (\mathcal{H}, w) - \frac{1}{C_a} (\mathcal{H}_x, w_x) \right. \\ \left. + (c^2 s_x, \psi_x) + \frac{\gamma}{C_a} ((h_x, \psi_x) - (B_o h, \psi)) \right) dt.$$

2.3. Boundedness of weak form and disjoining pressure assumptions.

We now discuss the boundedness of the weak formulation, in particular suitable choices of the disjoining pressure $\phi'(h)$. First note that all the terms in the bilinear form $\mathcal{A}(\cdot, \cdot)$ can be shown to be bounded within the indicated function spaces (by using Cauchy-Schwarz inequalities). Next, observe that the time derivative terms $\langle h_t, v \rangle$ and $\langle s_t, \psi \rangle$ are bounded because $h_t, s_t \in H^1(\Omega)^*$ and $v, \psi \in H^1(\Omega)$. Furthermore, the term $(\frac{1}{3} h^3 \mu_x, v_x)$ can be bounded as follows:

$$(2.12) \quad |(h^3 \mu_x, v_x)| \leq \|h\|_{L^\infty(\Omega)}^3 \|\mu_x\|_{L^2(\Omega)} \|v_x\|_{L^2(\Omega)} \leq C \|h\|_{H^1(\Omega)}^3 \|\mu\|_{H^1(\Omega)} \|v\|_{H^1(\Omega)},$$

for all $h, \mu, v \in H^1(\Omega)$, where in the last step we used a Sobolev embedding inequality (in 1D).

Finally, to ensure that the term $(\phi'(h), w)$ is bounded, we assume for simplicity that $\phi \in C^1(\mathbb{R})$, and satisfies the following Lipschitz condition:

$$(2.13) \quad |\phi'(\xi) - \phi'(\zeta)| \leq C_L |\xi - \zeta|, \quad \forall \xi, \zeta \in \mathbb{R},$$

which implies (see Appendix B for the full proof):

$$(2.14) \quad |(\phi'(h), w)| \leq C_L (\|h\|_{L^2(\Omega)} + C) \|w\|_{L^2(\Omega)}, \quad \forall h, w \in L^2(\Omega) \supset H^1(\Omega),$$

where C_L is the Lipschitz constant and $C = |h_\star|$ is a constant that depends on the value of h_\star , which makes $\phi(h_\star) = 0$.

A common physically-motivated choice for $\phi(h)$ in the literature is (e.g., [35])

$$(2.15) \quad \phi(h) = -\frac{A}{2}h^{-2} \quad \Rightarrow \quad \phi'(h) = Ah^{-3},$$

where A is the nondimensional Hamaker constant. This choice does not satisfy the Lipschitz condition and is not bounded, which causes the model (2.2) to break down when the film ruptures, i.e., $h^{-1}(x) \rightarrow \infty$ for some $x \in \Omega$. A common way in the literature to deal with that is to regularise $\phi(h)$. We adopt the approach proposed in [22] (see also [37]) as follows:

$$(2.16) \quad \phi(h) = \begin{cases} \frac{A}{2\varepsilon^4}h^2 - \frac{A}{\varepsilon^2} & \text{if } h < \varepsilon, \\ -\frac{A}{2}h^{-2} & \text{if } h \geq \varepsilon. \end{cases}$$

The idea is to use a small $\varepsilon > 0$ to make $\phi(h)$ quadratic for $h < \varepsilon$, while keeping its form as $\phi(h) = -\frac{A}{2}h^{-2}$ for $h \geq \varepsilon$, ensuring that $\phi(h)$ has a minimum at $h = 0$. The adopted approach also ensures that $\phi(h)$ and $\phi'(h)$ are continuous at all points, particularly at $h = \varepsilon$.

3. Optimal control problem. We formulate an optimal control problem for the thin film flow dynamics over a flexible topography (2.10). Our goal is to find a distributed force $f(x, t)$ that influences the topography $s(x, t)$ as in (2.2c) so that the optimal solution approaches the target state $\bar{h}(x)$. This optimal solution is either the height of the thin film $h(x, t)$ or the total observed surface $\mathcal{H}(x, t) = h(x, t) + s(x, t)$.

Formally, we seek a distributed force $f(x, t)$ that minimises the cost function $\bar{\mathcal{J}}(h, s, f)$:

$$(3.1) \quad \bar{\mathcal{J}}(h, s, f) := \frac{1}{2} \|(h + \beta s)(\cdot, T) - \bar{h}(\cdot)\|_{L^2(\Omega)}^2 + \frac{\alpha}{2} \int_0^T \|f(\cdot, t)\|_{L^2(\Omega)}^2 dt,$$

where $\beta \in \{0, 1\}$ and $\alpha > 0$ is a regularisation parameter. The first term in equation (3.1) measures the difference between the current state and the target state \bar{h} , while the second term, determines a penalty for the control energy. In the unconstrained control setting of this paper, this control penalty is crucial for ensuring the problem's well-posedness [24]. We formulate the optimal control problem as:

$$(3.2) \quad \min_{(h, s, f)} \bar{\mathcal{J}}(h, s, f), \quad \text{subject to (2.10)}.$$

3.1. First-order optimality conditions. In this work, we follow an ‘‘optimise-then-discretise’’ approach that generally ensures computational robustness and mesh independence, effectively addressing numerical challenges in problems with low regularity multipliers and improving convergence behaviour [12]. We begin by deriving first-order optimality conditions for (3.2). For this, we define the Lagrangian

$$(3.3) \quad \begin{aligned} \mathcal{L}((h, \mu, s), f, (p, q, r)) &:= \bar{\mathcal{J}}(h, s, f) + \int_0^T \langle h_t, p \rangle + \langle s_t, r \rangle dt \\ &+ \int_0^T \left(\frac{1}{3} h^3 \mu_x, p_x \right) - (f, r) - (\phi'(h), q) dt + \mathcal{A} \left((h, \mu, s), (p, q, r) \right). \end{aligned}$$

The optimality conditions arise from stationarity conditions of this Lagrangian with respect to state, adjoint, and control variables (see Chapter 3 in [12] and [1] for

further details). Consequently, the adjoint problem consists in finding $(p, q, r) \in \mathcal{W}^{h(T)} \times \mathcal{V} \times \mathcal{W}^{\beta s(T)}$ solving

$$(3.4) \quad - \int_0^T \left(\langle p_t, v \rangle + \langle r_t, \psi \rangle + (\phi''(h)q, w) - (h^2 \mu_x p_x, v) + \left(\frac{1}{3} h^3 p_x, w_x \right) \right) dt \\ + \mathcal{A}((v, \omega, \psi), (p, q, r)) = \int_0^T (r, \psi) dt,$$

where $\mathcal{W}^{v_T} := \{v \in \mathcal{W} : v(T) = v_T\}$. The optimality conditions (3.4) can be expressed as a forward-backwards system. In other words, the optimal state variables, (h^*, μ^*, s^*) , and the corresponding optimal adjoint variables, (p^*, q^*, r^*) , satisfy the following strong form:

$$(3.5a) \quad \begin{cases} h_t^* - \frac{1}{3} (h^{*3} \mu_x^*)_x = 0, \\ \mu^* = \phi'(h^*) - \frac{B_o}{C_a} (\mathcal{H}^*) - \frac{1}{C_a} (\mathcal{H}_{xx}^*), \\ s_t^* - c^2 s_{xx}^* - \frac{\gamma}{C_a} (h_{xx}^* + B_o h^*) = f^*, \end{cases}$$

$$(3.5b) \quad \begin{cases} -p_t^* + h^{*2} \mu_x^* p_x^* + \frac{1}{C_a} (q_{xx}^* + \gamma r_{xx}^*) + \frac{B_o}{C_a} (q^* - \gamma r^*) - \phi''(h^*) q^* = 0, \\ \left(-\frac{1}{3} h^{*3} p_x^* \right)_x + q^* = 0, \\ -r_t^* - c^2 r_{xx}^* + \frac{B_o}{C_a} q^* + \frac{1}{C_a} q_{xx}^* = 0, \end{cases}$$

$$(3.5c) \quad \begin{cases} h_x^* = \mu_x^* = s_x^* = p_x^* = q_x^* = r_x^* = 0, & \text{on } \Omega \times [0, T], \\ h^* = h_0, \quad s^* = s_0, & \text{on } \Omega \times \{t = 0\}, \\ p^* = r^* = (\bar{h} - (h + \beta s)), & \text{on } \Omega \times \{t = T\}. \end{cases}$$

closed by the optimality condition

$$(3.6) \quad \alpha f^* - r^* = 0.$$

3.2. Reduced gradient approach. We solve the optimisation problem (3.2) by means of gradient descent. For this, the system dynamics (2.2) are used to define a nonlinear map from f to $h + \beta s$, leading to a reduced objective functional \mathcal{J} expressed solely in terms of f :

$$(3.7) \quad \mathcal{J}(f) = \bar{\mathcal{J}}(h(f), s(f), f) = \frac{1}{2} \|(h + \beta s)(f; \cdot, T) - \bar{h}(\cdot)\|_{L^2(\Omega)}^2 + \frac{\alpha}{2} \int_0^T \|f(\cdot, t)\|_{L^2(\Omega)}^2 dt.$$

Here, $(h + \beta s)(f; \cdot, t)$ represents the solution of the system (2.2) for a given f . Expressed in terms of the reduced objective functional, the optimal control problem can be reformulated as follows:

$$(3.8) \quad \min_f \mathcal{J}(f), \quad \text{subject to (2.2).}$$

```

Require: tol > 0,  $k_{\max}$ ,  $f^0$ ,  $\lambda$ ,  $k = 0$ ;
1: while  $\|\nabla \mathcal{J}(f^k)\| > \text{tol}$  and  $k < k_{\max}$  do
2:   Obtain  $(h^k, \mu^k, s^k)$  with  $f^k$  from (3.5a).
3:   Obtain  $(p^k, q^k, r^k)$  with  $(h^k, \mu^k, s^k)$  from (3.5b).
4:   Evaluate the gradient  $\nabla \mathcal{J}(f^k)$  from (3.6).
5:   Update  $f^{k+1} = f^k - \lambda^k \nabla \mathcal{J}(f^k)$ 
6:   while  $\mathcal{J}(f^{k+1}) > \mathcal{J}(f^k)$  do
7:     Obtain  $(h^{k+1}, \mu^{k+1}, s^{k+1})$  with  $f^{k+1}$ 
8:     Evaluate the cost  $\mathcal{J}(f^{k+1})$ 
9:     if  $\mathcal{J}(f^{k+1}) > \mathcal{J}(f^k)$  then
10:       $\lambda^m = 0.5\lambda^k$ ,  $m \geq k$ 
11:      Update  $f^{k+1} = f^k - \lambda^m \nabla \mathcal{J}(f^k)$ 
12:     end if
13:   end while
14:    $k := k + 1$ 
15: end while

```

Fig. 2: Gradient descent method with backtracking line search.

It can be shown (see, e.g., Chapter 4 of [12]), that the gradient of the reduced objective can be recovered from the optimality condition (3.6), that is,

$$(3.9) \quad \nabla \mathcal{J}(f) := \alpha f - r,$$

where the adjoint variable r is to be computed from the forward-backward system (3.5) which depends on f through the state equation. This gradient is the used in the iteration

$$(3.10) \quad f^{(k+1)} = f^{(k)} - \lambda^{(k)} \nabla \mathcal{J}(f^k), \quad k = 1, 2, \dots$$

where the stepsize λ^k is computed by backtracking. An elementary version of the pseudocode for this iterative loop is outlined in Figure 2.

4. Numerical approximation and tests.

4.1. IMEX-FEM discretisation of the model. For the computational treatment, the optimality conditions (3.5)-(3.6) derived above at a continuous level are discretised in space using the standard Finite Element Method (FEM) for variables h, s, f , and μ , as well as the adjoint variables p, q , and r , subject to homogeneous Neumann boundary conditions. More details on the FEM formulation are provided in Appendix C. For the time discretisation we need more careful treatment as the nonlinearities in equations (2.11) and (3.4) require a particular choice for the time-discretisation scheme to balance computational efficiency and stability [52]. We explore first-order Implicit-Explicit (IMEX) time-stepping schemes, which decompose the nonlinear term ϕ in (2.15) as:

$$(4.1) \quad \phi(h; v) = \phi_+(h; v) + \phi_-(h; v),$$

where ϕ_+ and ϕ_- denote the contractive (convex) and expansive (concave) components, respectively. The IMEX scheme treats the convex part implicitly and the

concave part explicitly. The time interval $[0, T]$ is divided into N smaller intervals $0 = t_0 < t_1 < \dots < t_N = T$, with each sub-interval $\mathcal{I}_{k+1} = [t_k, t_{k+1}]$ having a uniform time step $\Delta t = t_{k+1} - t_k$ for $k = 0, 1, \dots, N-1$. The time discretisation for problem (2.11) is:

Find $(h_{k+1}, \mu_{k+1}, s_{k+1}) \in \mathcal{V} \times \mathcal{V} \times \mathcal{V}$ such that for all $(v, \omega, \psi) \in \mathcal{V} \times \mathcal{V} \times \mathcal{V}$

$$(4.2) \quad \begin{aligned} & \left(\frac{h^{k+1} - h^k}{\Delta t}, v \right) + \left(\frac{s^{k+1} - s^k}{\Delta t}, \psi \right) - (\phi'_+(h^{k+1}); v) - (\phi'_-(h^k); v) \\ & + \left(\frac{1}{3} (h^k)^3 \mu_x^{k+1}, v_x \right) + \mathcal{A}((h^{k+1}, s^{k+1}, \mu^{k+1}), (v, \omega, \psi)) = (f^{k+1}, \psi), \end{aligned}$$

for $k = 0, 1, \dots, N-1$, where the initial condition is

$$(h, v) = (h_0, v) \quad \text{and} \quad (s, \psi) = (s_0, \psi), \quad \forall v, \psi \in L^2(\Omega).$$

It can be shown that this scheme dissipates the total energy (2.5) using techniques shown in [52].

For the adjoint problem (3.4), we introduce an IMEX time-stepping scheme to discretise backwards in time:

Find $(p_k, q_k, r_k) \in \mathcal{V} \times \mathcal{V} \times \mathcal{V}$ such that for all $(v, \omega, \psi) \in \mathcal{V} \times \mathcal{V} \times \mathcal{V}$

$$(4.3) \quad \begin{aligned} & - \left(\frac{p^{k+1} - p^k}{\Delta t}, v \right) - \left(\frac{r^{k+1} - r^k}{\Delta t}, \psi \right) - (\phi''_+(h^{k+1})q^{k+1}, w) - (\phi''_-(h^k)q^k, w) \\ & - ((h^k)^2 \mu_x^{k+1} p_x^{k+1}, v) + \frac{1}{3} ((h^k)^3 p_x^{k+1}, w_x) - (r^{k+1}, \psi) \\ & + \mathcal{A}((p^k, q^k, r^k), (v, \omega, \psi)) = 0, \end{aligned}$$

for $k = 0, 1, 2, \dots, N-1$, where the terminal condition is:

$$(4.4) \quad \begin{aligned} & (p^N, v) + (r^N, \psi) - \Delta t (\phi''_+(h^N), q^N) + \frac{\Delta t}{3} ((h^N)^3 p_x^N, v) \\ & + \Delta t \mathcal{A}((p^N, q^N, r^N), (v, \omega, \psi)) = (\bar{h}^N - (h + \beta s)^N, v). \end{aligned}$$

4.2. Numerical tests. The results were generated using the forward-backward optimisation algorithm (Figure 2) with a tolerance $\text{tol} = 10^{-4}$ and initial guess $f^0 = 0$. All simulations were carried out using a space-time discretisation with $n = 250$ nodes, a time step $\Delta t = 0.05$, and the following fixed parameters: $C_a = B_o = 1$, $c = 0.1$, $\gamma = 0$, and $\alpha = 10^{-6}$. We solve the system (3.5) on $[0, L]$ and extend the solution symmetrically to $[-L, L]$ for visualisation purposes. The initial conditions used in the numerical simulations are, unless otherwise specified,

$$(4.5) \quad h_0(x) = 1 + h_A \cos\left(\frac{m\pi x}{L}\right), \quad s_0(x) = 0,$$

where the initial amplitude h_A will generally be chosen between $[0, 0.5]$ (with $h_A = 0$ corresponding to a flat state), and the frequency parameter will be set to $m = 1$ unless otherwise specified. We note that the respective flow with a flat substrate evolves to a nontrivial state whenever $L > 2\pi$, as predicted by linear stability analysis [23]. In addition to utilising the cost function and the norm of its gradient to validate our solution, we also employ the L_∞ -norm as a measure of accuracy; it is defined as $\max_{t \in [0, T]} \|(h^*(t) + \beta s^*(t)) - \bar{h}\|_\infty$.

4.3. Non-rupture scenarios. In this section, we set $\beta = 1$ in (3.7) because our goal is to control the observed surface, defined as $\mathcal{H} = h + s$.

4.3.1. Accelerated transition to desirable surface shape. We begin the presentation by comparing the time required for uncontrolled and controlled free surfaces to reach a steady state. For the uncontrolled case (i.e., $s = f = 0$), the forward system (2.2) has been resolved by [23] for $L = 3\pi$, and reached a steady state after $T = 900$ time units. We aim to observe how fast the optimal state \mathcal{H}^* approaches the target state \bar{h} when control is applied.

We apply the forward-backwards optimisation method using the algorithm in Figure 2, where control is applied at the final time $T = 5$, using initial conditions (4.5) with $h_A = 0.5$. The result of this computation is demonstrated in Figures 4 and 5. The steady state is exported as our target state \bar{h} , shown in panel 4a. The optimal free surface over topography, \mathcal{H}^* , shown in panel 4b, successfully achieves this target state fast. The plot in panel 4c illustrates how the optimal free surface, h^* , varies over time. Panel 4d shows the topography s^* evolving from a flat state to an optimally adjusted profile with unexpected peaks and troughs, while panel 4e shows the control parameter f^* exhibits oscillatory behaviour to shape the optimal topography s^* . The cost function $\mathcal{J}(f^*)$ illustrated in panel 4f, decreases to zero by the final time. Lastly, Figure 5a shows the infinity norm of the controlled solution $(h^*(t) + \beta s^*(t)) - \bar{h}$ goes to zero much faster than the uncontrolled one, and Figure 5b explores the impact of the regularisation parameter α on the solution, showing that smaller values of α than 10^{-3} lead to negligible changes to the optimal solution.

It is noteworthy to mention that, to ensure that \mathcal{H}^* remains in a steady state, the optimal solution \mathcal{H}^* and the topography s^* are utilised as the initial conditions in the forward system (2.2). As expected, the free surface remains unchanged and the topography transitions towards a flat state.

We extend the first example by solving the forward system (2.2) over a non-flat topography, contrasting with the flat substrate examined previously. The uncontrolled system is solved with initial conditions comprising a flat surface profile (i.e., using $h_A = 0$) and a substrate profile $s_0(x) = a \left(\tanh\left(\frac{x+c_1}{d}\right) - \tanh\left(\frac{x-c_2}{d}\right) \right)$, where $a = -0.25$, $c_1 = -0.35L$, $c_2 = 0.65L$, $L = 3\pi$, and the topography steepness is $d = -0.2$. The aim remains the same as in the first example in achieving the target state much faster than the uncontrolled one. A steady state for the free surface is achieved and the optimal control solution is presented in Figures 6 and 7. Panel 7a shows the target state, and panels 7b and 7c illustrate the time evolution of \mathcal{H}^* and h^* , respectively. The smoothing changes in amplitudes and phases of s^* are highlighted in panel 7d, and the oscillatory forces f^* that influence s^* are shown in panel 7e. Figure 8 demonstrates that both the L^∞ norm and the cost function converge to zero, although the convergence is slower than the case with a flat initial topography.

The final example of this section considers a case where the free surface quickly transitions from flat to a desired wave-like shape in a short time $t = [0, 1]$, as shown in Figures 9 and 10. Using a computational domain of length $L = 5$, we start with an initially flat surface by setting $h_A = 0$ in (4.5). Without control, the surface remains flat, but with control, it transforms into the desired wave-like shape as shown in Figure 10a. The optimal solution of \mathcal{H}^* and h^* are shown in panels 10b and 10c, respectively. The topography s^* changes from flat to an oscillatory profile, enabling the desired wave-like target state. The control force f^* oscillates in sync with the topography changes, facilitating rapid adaptation, as seen in panel 10e. Figure 11 demonstrates the cost function decreases towards zero, achieving the minimum cost,

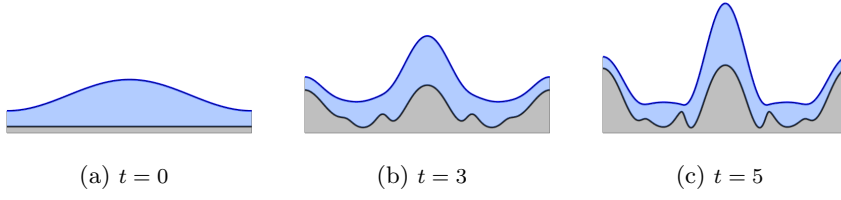


Fig. 3: Snapshots of the optimal solution, controlled to a desired surface shape. The solution is extended symmetrically in domain $[-L, L]$.

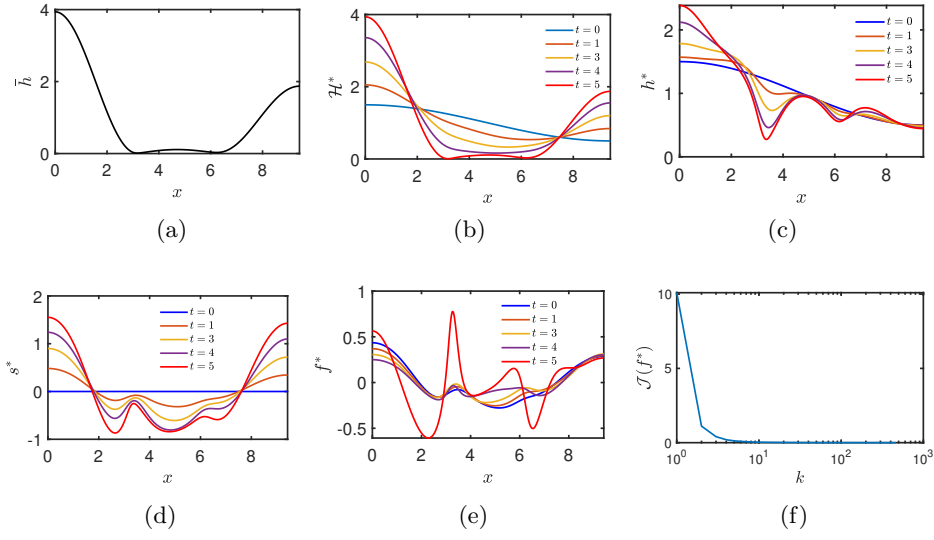


Fig. 4: (a) Target state \bar{h} . (b-e) Evolution of the optimal surface profile \mathcal{H}^* , film height h^* , topography s^* , and control f^* , respectively. (f) Cost function $\mathcal{J}(f^*)$ against number of iterations k .

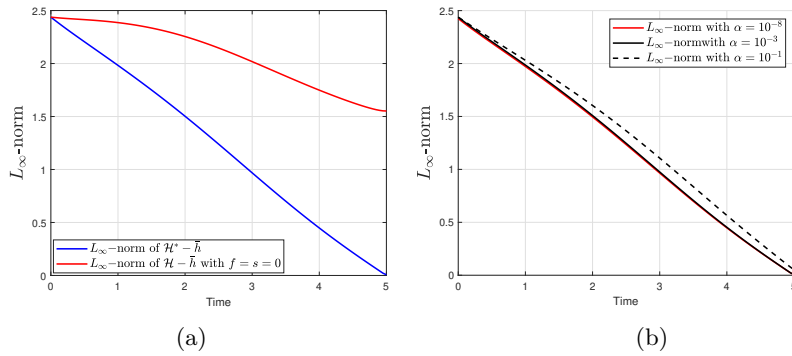


Fig. 5: L^∞ -norms for (a) the controlled and uncontrolled solutions, and (b) various values of α .

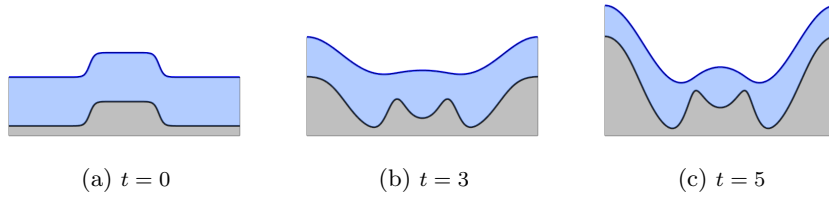


Fig. 6: Snapshots of the optimal solution, controlled to a desired surface shape.

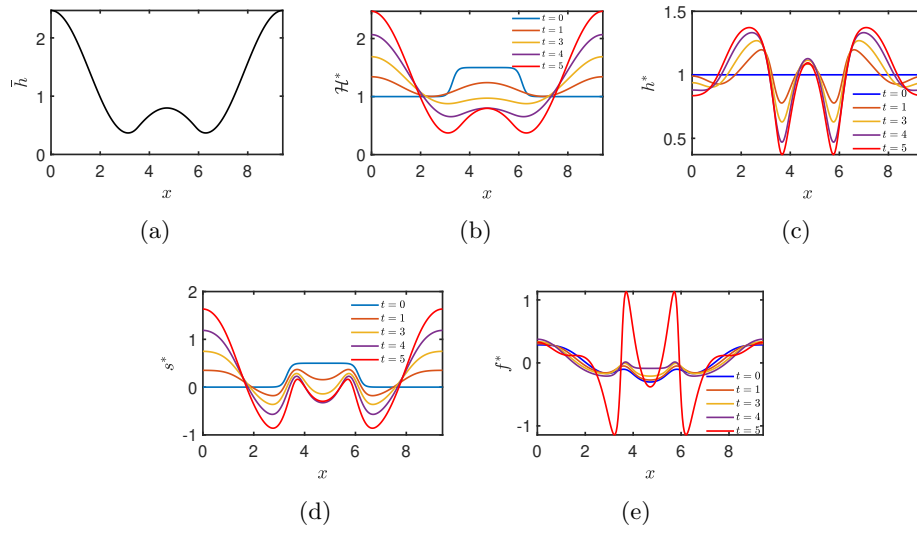


Fig. 7: (a) Target state \bar{h} . (b-e) Evolution of the optimal surface profile \mathcal{H}^* , film height h^* , topography s^* , and control f^* , respectively.

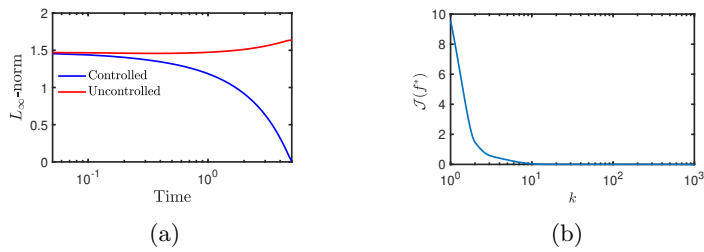


Fig. 8: (a) L^∞ -norm for the controlled and uncontrolled solutions. (b) Cost function $\mathcal{J}(f^*)$ against number of iterations k .

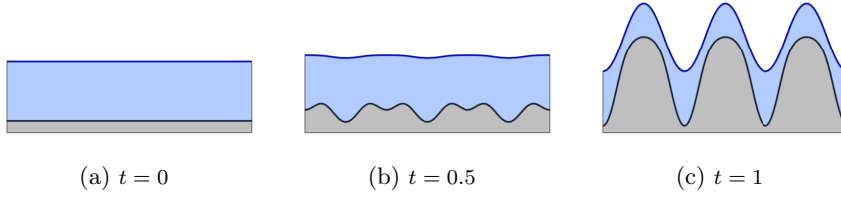


Fig. 9: Snapshots of the optimal solution, controlled to a desired surface shape. The solution is extended symmetrically in domain $[-L, L]$.

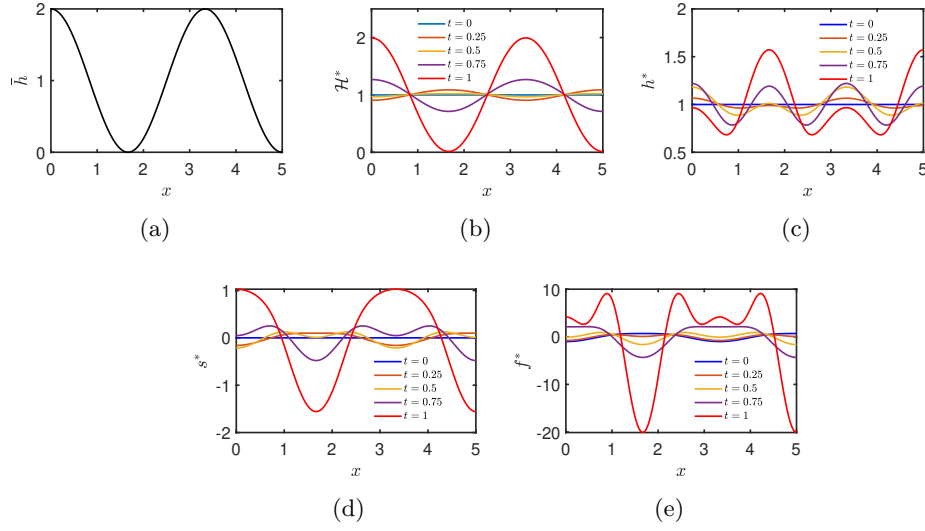


Fig. 10: (a) Target state \bar{h} . (b-e) Evolution of the optimal surface profile \mathcal{H}^* , film height h^* , topography s^* , and control f^* , respectively.

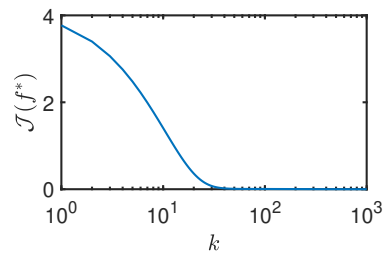


Fig. 11: Cost function $\mathcal{J}(f^*)$ against number of iterations k .

and the optimal control reaches the target surface.

4.3.2. From non-flat to desired shapes. The next example follows the work of [26] where a related (uncontrolled) evolution equation for thin-film flow over topography was solved and a non-flat steady state was achieved. We initiate our control problem using one of these non-flat states as the initial condition by taking $h_0(x) = 1 + 10 \exp(-(2x)^2)$, $s_0(x) = 0$, and set $L = 10$, $B_o = 0$. Our aim is to control the problem and flatten the surface (i.e., the target state is $\bar{h} = 1$). The time evolution of the various system variables is shown in Figures 12 and 13. Panel 13b shows that our optimal solution achieves a flat state, while panel 13c displays deviations in h^* indicating it cannot be a flat alone. Panels 13d and 13e reveal s^* and f^* adapting by $T = 5$ to counterbalance the variations in h^* , aligning $\mathcal{H}^* = h^* + s^*$ with the target state. Figure 14 shows the L^∞ -norm for the controlled and uncontrolled solutions over time, relative to the target state. The controlled solution moves towards zero, while the uncontrolled solution stabilises at a non-zero value.

We also carried out simulations aiming to retain the surface at a linear state, while solving the nonlinear system (recall that this exhibits free-surface instabilities in the uncontrolled case if $L > 2\pi$). The solution of the uncontrolled forward system with initial conditions (4.5) and $h_A = 0.5$, $m = 3$, $L = \frac{15}{2}\pi$ results in nonlinear instability, but our objective is to maintain the free surface at the linear initial condition $\mathcal{H}(x, 0) = h_0 + s_0$ (i.e., $\bar{h} = \mathcal{H}(x, 0)$) throughout the simulation period $[0, T]$, with final simulation time $T = 10$. The results of the computation are depicted in Figures 15, 16 and 17. Panel 16a shows the target state \bar{h} , whereas panel 16b presents \mathcal{H}^* maintaining its initial sinusoidal shape. Panel 16c depicts the free surface evolution, which naturally tends towards instability (non-flat state). In contrast, it is adjusted by the changing topography in panel 16d, which develops inverse undulations to h^* to maintain \mathcal{H}^* . The oscillatory behaviour of the control f^* is depicted in panel 16e. The cost function decreases as indicated in panel 16f, reflecting progress towards the target state. Finally, Figure 17 shows a brief increase in the infinity norm due to strong instability, before it returns to near zero.

4.4. Rupture scenarios. In this section, we set $\beta = 0$ in (3.7), focusing on controlling $h(x, t)$ rather than the total surface $\mathcal{H} = h + s$. This approach lets \mathcal{H} rupture naturally, driven by the interaction between the thin film $h(x, t)$ and the underlying topography $s(x, t)$, providing a realistic representation of physical rupture. If we were to control \mathcal{H} directly, it could prevent rupture by limiting the film's ability to interact with the topography closely.

In the following examples, we aim to examine how thin-film flows evolve towards a rupture state. We set a non-zero rupture function $\phi(h)$ as in (4.1), with $\phi_+ = \frac{1}{2\epsilon^4}h^2$, $\epsilon = 0.1$, and $A = 0.03$. In order to obtain a ruptured steady state, \bar{h}_{rupt} , the forward system (2.2) is first solved on a flat substrate ($s = 0$), using the initial conditions (4.5) with $h_A = 0.5$. The simulations are carried out over $[0, T]$, with $T = 550$, and within a spatial domain of length $L = 3\pi$.

In the first example, we assess how quickly the optimal free surface h^* reaches the target rupture state $\bar{h} = \bar{h}_{\text{rupt}}$, relative to the uncontrolled case. The optimal solution is shown in Figures 18 and 19. While the uncontrolled solution necessitated $T = 550$ to achieve a steady ruptured thin-film state \bar{h}_{rupt} , shown in panel 19a, our controlled solution h^* achieves the desired state within just $T = 30$, as seen in panel 19b. Panel 19c depicts how the optimal thin-film flow over topography \mathcal{H}^* , including rupture effects, changes over time. The optimal topography s^* , and the control function f^* are illustrated in panels 19d and 19e, respectively. The significant

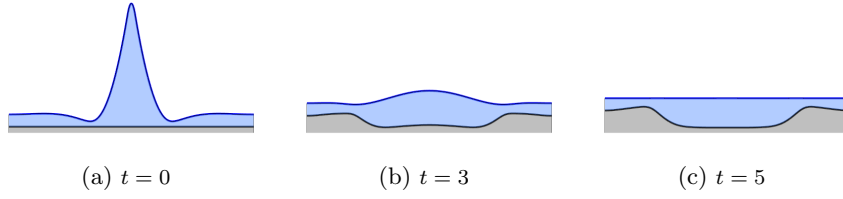


Fig. 12: Snapshots of the optimal solution, controlled to a uniform state. The solution is extended symmetrically in domain $[-L, L]$.

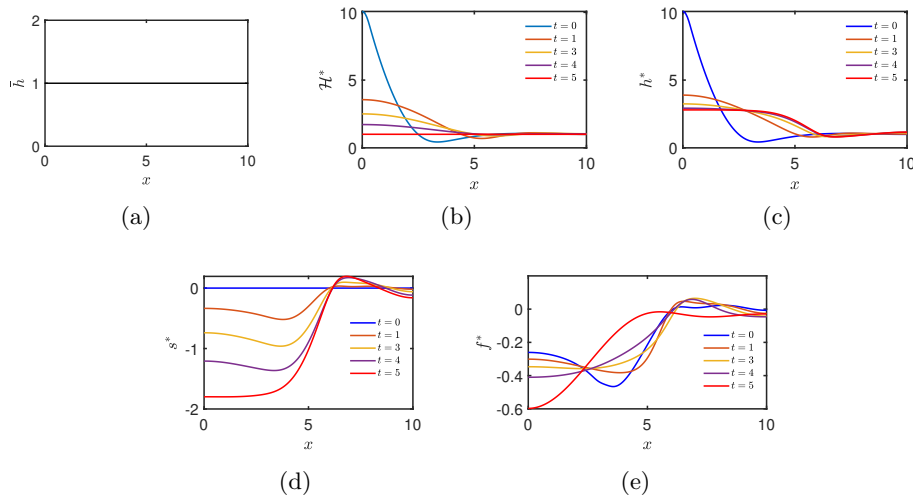


Fig. 13: (a) Target state \bar{h} . (b-e) Evolution of the optimal surface profile \mathcal{H}^* , film height h^* , topography s^* , and control f^* , respectively.

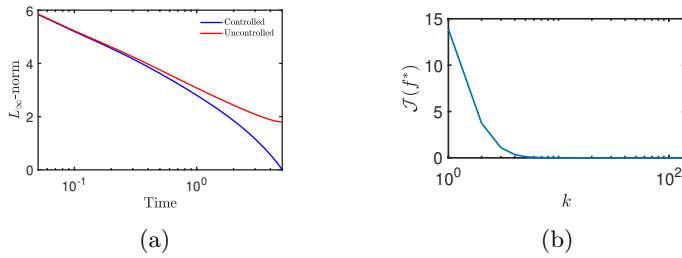


Fig. 14: (a) L^∞ -norm for controlled and uncontrolled solutions. (b) Cost function $\mathcal{J}(f^*)$ against number of iterations k .

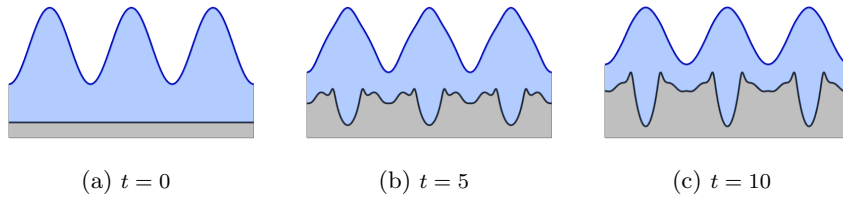


Fig. 15: Snapshots of the optimal solution, controlled to remain at the initial surface shape. The solution is extended symmetrically in domain $[-L, L]$.

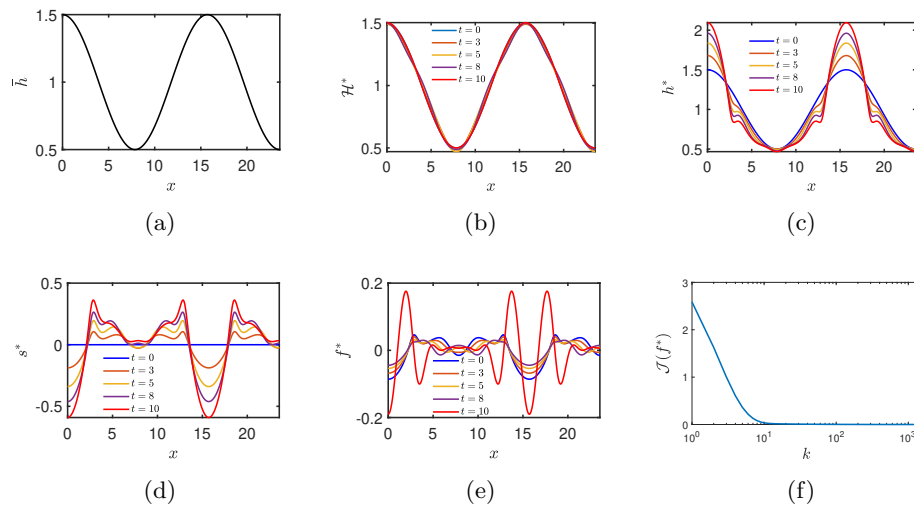


Fig. 16: (a) Target state \bar{h} . (b-e) Evolution of the optimal surface profile \mathcal{H}^* , film height h^* , topography s^* , and control f^* , respectively. (f) Cost function $\mathcal{J}(f^*)$ against number of iterations k .

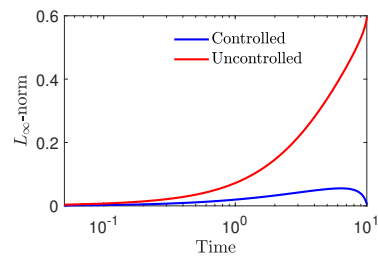


Fig. 17: L^∞ -norm of controlled vs uncontrolled solutions relative to \bar{h} .

reduction in convergence time is highlighted in Figure 20. Both L^∞ norm of $h^* - \bar{h}_{rupt}$ and cost function approach zero, though more slowly than in the non-rupture case.

In the final example, we start with an initially ruptured state, $h_0(x) = \bar{h}_{rupt}$, and show that our control can halt the rupture by allowing the bubbles to merge into a single uniform surface, as shown in Figure 21. This demonstrates how control can guide the system from rupture to a stable state. Figure 22 depicts h^* , \mathcal{H}^* , the flexible topography s^* and control f^* , as well as the cost function which is seen to reach its minimum faster compared to the previous example (cf. Figure 20b).

5. Discussion. We have developed a mathematical framework for the open-loop optimal control of thin-film flows over flexible topography, accounting for the rupture of films and the coalescence of bubbles. The focus of this study has been on finding the distributed force influencing the flexible topography to minimise the cost function. We have also established a functional setting for the coupled PDE system, comprising a thin film equation and a flexible substrate equation. This demonstrates that this system adheres to a global energy-dissipation law. Furthermore, we have derived the optimality conditions by formulating the mathematical control problem as a PDE-constrained optimisation to obtain the time-dependent forward and backward PDE system and the optimality condition. We used a stable time discretisation approach with (IMEX) schemes to address the model's nonlinearity, such as the disjoining-pressure term. This approach worked well in our numerical examples, demonstrating its effectiveness in solving the optimisation problem.

The effectiveness of our optimal control problem was demonstrated through a range of numerical examples, showing its ability to accelerate convergence to steady states, stabilise dewetting processes, achieve specific profiles, and even reverse rupture dynamics to restore uniformity. These results were achieved by allowing the adjacent wall to take a flexible shape, thereby affecting the surface profile. This non-standard approach provides a mechanism to control thin-film dynamics without altering the fluid properties (e.g., surface tension, stresses). It offers a useful alternative for addressing challenges in thin-film control and complements existing control approaches; previous studies have focussed on using thermal feedback [17, 45], fluid injection and extraction [10, 21, 31, 46], or electric fields [47, 51].

The optimality system presented in this study was formulated as an open-loop control problem, namely the controller design is independent of the system output. This work can be extended to closed-loop control, also known as feedback control, which influences the control input directly [4] and helps navigate the system along the optimal path set by the open-loop control problem [32]. In thin film applications, feedback control not only stabilises contact line instabilities but also addresses complex problems, such as optimising the placement of actuators and sensors to suppress or enhance waves on a thin film [17, 21, 46]. In addition, feedback control using fluid injection and extraction techniques are employed to mitigate wave phenomena in thin films and optimise actuator placement [25, 46]. The extension of our work to feedback control and developing numerical methods for solving a closed-loop control problem is left as future work.

Acknowledgments. SA acknowledges the financial support from Islamic University of Madinah and Ministry of Education of Saudi Arabia. The research by KvdZ was supported by the Engineering and Physical Sciences Research Council (EPSRC), UK under Grant and EP/W010011/1.

Appendix A. Free energy dissipation. Here we derive the identity (2.6). We recall the energy

$$(A.1) \quad \mathcal{E} = \int_{\Omega} \left[\phi(h) + \frac{1}{2C_a} h_x^2 + \frac{c^2}{2\gamma} s_x^2 + \frac{1}{C_a} h_x s_x - \frac{B_0}{2C_a} h^2 - \frac{B_0}{C_a} h s \right] dx.$$

The goal is to derive the rate of change of this energy in time

$$(A.2) \quad \frac{d\mathcal{E}}{dt} = \frac{d}{dt} \int_{\Omega} \left[\phi(h) + \frac{1}{2C_a} h_x^2 + \frac{c^2}{2\gamma} s_x^2 + \frac{1}{C_a} h_x s_x - \frac{B_0}{2C_a} h^2 - \frac{B_0}{C_a} h s \right] dx.$$

We apply the chain rule and integrate by parts on the terms involving spatial derivatives, then apply the boundary conditions (2.4) to remove the boundary terms, yielding

$$(A.3) \quad \frac{d\mathcal{E}}{dt} = \int_{\Omega} \left[\left(\phi'(h) - \frac{1}{C_a} h_{xx} - \frac{B_0}{C_a} h \right) h_t - \frac{c^2}{\gamma} s_{xx} s_t + \frac{1}{C_a} (h_x s_x)_t - \frac{B_0}{C_a} (h s)_t \right] dx.$$

We use equations (2.2) to simplify the above expression, resulting in the dissipation law

$$(A.4) \quad \frac{d}{dt} \mathcal{E}(h, s) = - \left(\frac{1}{3} \int_{\Omega} h^3 \mu_x^2 dx + \frac{1}{\gamma} \int_{\Omega} s_t^2 dx \right) + \frac{1}{\gamma} \int_{\Omega} f s_t dx.$$

This equation represents the rate of change of the free energy. The first term on the right-hand side corresponds to the dissipation in the fluid, the second term represents dissipation in the substrate, and the last term accounts for the work done by the external force on the substrate. Thus, without external forces (i.e., $f = 0$), the total free energy is non-increasing in time.

Appendix B. Boundedness of $(\phi'(h), w)$. We aim to prove the following inequality for any $h, w \in L^2(\Omega)$:

$$(B.1) \quad |(\phi'(h), w)| \leq C_L (\|h\|_{L^2(\Omega)} + C) \|w\|_{L^2(\Omega)}.$$

We write $\phi'(h)$ as

$$(\phi'(h), w) = (\phi'(h) - \phi'(h_{\star}), w) + \phi'(h_{\star}), w),$$

where h_{\star} is any fixed reference. Applying the Lipschitz condition and Hölder's inequality, we bound the expression

$$\begin{aligned} |(\phi'(h) - \phi'(h_{\star}), w)| &\leq C_L \int_{\Omega} |h(x) - h_{\star}| |w(x)| dx \\ &\leq C_L \|h - h_{\star}\|_{L^2(\Omega)} \|w\|_{L^2(\Omega)}. \end{aligned}$$

Since h_{\star} is a constant, we conclude

$$|(\phi'(h), w)| \leq C_L (\|h\|_{L^2(\Omega)} + |h_{\star}|) \|w\|_{L^2(\Omega)}.$$

Thus, we have

$$(B.2) \quad |(\phi'(h), w)| \leq C_L (\|h\|_{L^2(\Omega)} + C) \|w\|_{L^2(\Omega)},$$

where C_L is the Lipschitz constant and $C = |h_{\star}|$ is a constant that depends on the value of h_{\star} , which makes $\phi(h_{\star}) = 0$.

Appendix C. FEM space discretisation. We partition the subset $\Omega \subset \mathbb{R}$ into $n - 1$ elements with a total of n nodes. As a result, the space $V := H^1(\Omega)$ is replaced by a finite-dimensional subspace, $V_h \subset V$, which has a dimension of n . We employ piecewise-linear basis functions $\phi_i(x)$, $i = 1, \dots, n$. The solutions can therefore be characterised as linear combinations of ϕ_i with real coefficients, such that $\mathbf{F}(x, t) = \sum_{i=1}^n F_i(t)\phi_i(x)$. Here, \mathbf{F} represents a vector that holds the unknowns at each node and is one of the state, adjoint or control variables, i.e. $\mathbf{F} = \{\mathbf{h}, \boldsymbol{\mu}, \mathbf{s}, \mathbf{p}, \mathbf{q}, \mathbf{r}, \mathbf{f}\}$, with corresponding coefficients $F_i = \{h_i, \mu_i, s_i, p_i, q_i, r_i, f_i\}$.

We define the real $n \times n$ matrices

$$\begin{aligned} \mathbf{M}_{ij} &= \int_{\Omega} \phi_i(x)\phi_j(x) dx, & \mathbf{K}_{ij} &= \int_{\Omega} \phi'_i(x)\phi'_j(x) dx, \\ \hat{\mathbf{M}}_{ij}^k &= \int_{\Omega} m(h(t^k, x))\phi_i(x)\phi_j(x) dx, & \hat{\mathbf{K}}_{ij}^k &= \int_{\Omega} m(h(t^k, x))\phi'_i(x)\phi'_j(x) dx, \\ \hat{\mathbf{C}}_{ij}^k &= \int_{\Omega} m(h(t^k, x))\phi'_i(x)\phi_j(x) dx, & \mathbf{f} &= \int_{\Omega} f_i\phi_j(x) dx, \end{aligned}$$

where the primes denote derivatives with respect to x . Here, $m(h)$ can adopt forms such as h^2 or h^3 , determined by parameters such as $C(\mathbf{h}^2)$ or $\hat{K}(\mathbf{h}^3)$. Ultimately, we obtain the following discrete optimality system

$$(C.1a) \quad \begin{cases} \mathbf{M}\dot{\mathbf{h}}(t) + \frac{1}{3}\hat{\mathbf{K}}(\mathbf{h}^3) = 0, \\ \mathbf{M}\boldsymbol{\mu}(t) - \frac{A}{\epsilon^4}\hat{\mathbf{M}}(\phi'_+(\mathbf{h}))\mathbf{h}(t) - \frac{1}{C_a}(\mathbf{K} + B_o\mathbf{M})\boldsymbol{\mathcal{H}}(t) = \frac{A}{\epsilon^4}\hat{\mathbf{M}}(\phi'_-(\mathbf{h}))\mathbf{h}(t), \\ \mathbf{M}\dot{\mathbf{s}}(t) + c^2\mathbf{K}\mathbf{s}(t) + \frac{\gamma}{C_a}(\mathbf{K} - B_o\mathbf{M})\mathbf{h}(t) = \mathbf{M}\mathbf{f}, \end{cases}$$

$$(C.1b) \quad \begin{cases} -\mathbf{M}\dot{\mathbf{p}}(t) + \hat{\mathbf{C}}\mathbf{p}(t) + \left(\frac{B_o}{C_a}\mathbf{M} - \frac{1}{C_a}\mathbf{K} - \frac{A}{\epsilon^4}\hat{\mathbf{M}}(\phi''_+(\mathbf{h}))\right)\mathbf{q}(t) \\ \quad + \frac{\gamma}{C_a}(B_o\mathbf{M} - \mathbf{K})\mathbf{r}(t) = \frac{A}{\epsilon^4}\hat{\mathbf{M}}(\phi''_-(\mathbf{h}))\mathbf{q}(t), \\ \frac{1}{3}\hat{\mathbf{K}}(\mathbf{h}^3)\mathbf{p}(t) + \mathbf{M}\mathbf{q}(t) = 0, \\ -\mathbf{M}\dot{\mathbf{r}}(t) + c^2\mathbf{K}\mathbf{r}(t) - \frac{1}{C_a}(B_o\mathbf{M} - \mathbf{K})\mathbf{q}(t) = 0, \end{cases}$$

and the optimality condition

$$(C.2) \quad \alpha\mathbf{M}\mathbf{f}(t) - \mathbf{M}\mathbf{r}(t) = 0.$$

References.

- [1] G. ALBI, Y.-P. CHOI, M. FORNASIER, AND D. KALISE, *Mean field control hierarchy*, Applied Mathematics & Optimization, 76 (2017), pp. 93–135.
- [2] J. P. ALEXANDER, T. L. KIRK, AND D. T. PAPAGEORGIOU, *Stability of falling liquid films on flexible substrates*, Journal of Fluid Mechanics, 900 (2020), p. A40.
- [3] T. G. ANDERSON, R. CIMPEANU, D. T. PAPAGEORGIOU, AND P. G. PETROPOULOS, *Electric field stabilization of viscous liquid layers coating the underside of a surface*, Physical Review Fluids, 2 (2017), p. 054001.
- [4] B. AZMI, D. KALISE, AND K. KUNISCH, *Optimal feedback law recovery by gradient-augmented sparse polynomial regression*, Journal of Machine Learning Research (JMLR), 22 (2021).

- [5] D. BENNEY, *Long waves on liquid films*, Journal of mathematics and physics, 45 (1966), pp. 150–155.
- [6] F. BERNIS AND A. FRIEDMAN, *Higher order nonlinear degenerate parabolic equations*, Journal of differential equations, 83 (1990), pp. 179–206.
- [7] A. L. BERTOZZI AND M. PUGH, *The lubrication approximation for thin viscous films: the moving contact line with a 'porous media' cut-off of van der waals interactions*, Nonlinearity, 7 (1994), p. 1535.
- [8] J. BINARD, P. NOBLE, AND P. DEGOND, *Well-posedness and stability analysis of a landscape evolution model*, arXiv preprint arXiv:2211.09629, (2022).
- [9] M. BLYTH AND C. POZRIKIDIS, *Effect of surfactant on the stability of film flow down an inclined plane*, Journal of Fluid Mechanics, 521 (2004), pp. 241–250.
- [10] R. CIMPEANU, S. N. GOMES, AND D. T. PAPAGEORGIOU, *Active control of liquid film flows: beyond reduced-order models*, Nonlinear Dynamics, 104 (2021), pp. 267–287.
- [11] R. V. CRASTER AND O. K. MATAR, *Dynamics and stability of thin liquid films*, Reviews of modern physics, 81 (2009), p. 1131.
- [12] J. C. DE LOS REYES, *Numerical PDE-constrained optimization*, Springer, 2015.
- [13] M. M. DECREÉ AND J.-C. BARET, *Gravity-driven flows of viscous liquids over two-dimensional topographies*, Journal of Fluid Mechanics, 487 (2003), pp. 147–166.
- [14] M. A. DURÁN-OLIVENCIA, R. S. GVALANI, S. KALLIADASIS, AND G. A. PAVLIOTIS, *Instability, rupture and fluctuations in thin liquid films: Theory and computations*, Journal of statistical physics, 174 (2019), pp. 579–604.
- [15] P. D. FOWLER, C. RUSCHER, J. D. MCGRAW, J. A. FORREST, AND K. DALNOKI-VERESS, *Controlling marangoni-induced instabilities in spin-cast polymer films: How to prepare uniform films*, The European Physical Journal E, 39 (2016), pp. 1–8.
- [16] D. P. FRISK AND E. J. DAVIS, *The enhancement of heat transfer by waves in stratified gas-liquid flow*, International Journal of Heat and Mass Transfer, 15 (1972), pp. 1537–1552.
- [17] N. GARNIER, R. O. GRIGORIEV, AND M. F. SCHATZ, *Optical manipulation of microscale fluid flow*, Physical Review Letters, 91 (2003), p. 054501.
- [18] P. GASKELL, *Gravity-driven flow of continuous thin liquid films on non-porous substrates with topography*, Journal of Fluid Mechanics, 509 (2004), p. 253–280, <https://doi.org/10.1017/S0022112004009425>.
- [19] P. GASKELL, P. JIMACK, M. SELLIER, H. THOMPSON, AND M. WILSON, *Gravity-driven flow of continuous thin liquid films on non-porous substrates with topography*, Journal of Fluid Mechanics, 509 (2004), pp. 253–280.
- [20] M. V. GNANN AND M. PETRACHE, *The navier-slip thin-film equation for 3d fluid films: existence and uniqueness*, Journal of Differential Equations, 265 (2018), pp. 5832–5958.
- [21] S. N. GOMES, D. T. PAPAGEORGIOU, AND G. A. PAVLIOTIS, *Stabilizing non-trivial solutions of the generalized kuramoto–sivashinsky equation using feedback and optimal control: Lighthill–thwaites prize*, IMA Journal of Applied Mathematics, 82 (2017), pp. 158–194.
- [22] H. GOMEZ AND K. G. VAN DER ZEE, *Computational phase-field modeling*, in Encyclopedia of Computational Mechanics, Second Edition, E. Stein, R. de Borst, and T. J. R. Hughes, eds., Wiley, 2017. Part 1 Fluids.
- [23] P. S. HAMMOND, *Nonlinear adjustment of a thin annular film of viscous fluid surrounding a thread of another within a circular cylindrical pipe*, Journal of fluid

- Mechanics, 137 (1983), pp. 363–384.
- [24] R. HERZOG AND K. KUNISCH, *Algorithms for pde-constrained optimization*, GAMM-Mitteilungen, 33 (2010), pp. 163–176.
- [25] O. A. HOLROYD, R. CIMPEANU, AND S. N. GOMES, *Linear quadratic regulation control for falling liquid films*, SIAM Journal on Applied Mathematics, 84 (2024), pp. 940–960.
- [26] O. E. JENSEN, G. CHINI, AND J. KING, *Thin-film flows near isolated humps and interior corners*, Journal of engineering mathematics, 50 (2004), pp. 289–309.
- [27] A. KALOGIROU AND M. G. BLYTH, *Nonlinear dynamics of two-layer channel flow with soluble surfactant below or above the critical micelle concentration*, Journal of Fluid Mechanics, 900 (2020).
- [28] S. F. KISTLER AND P. M. SCHWEIZER, *Coating science and technology: An overview*, Liquid Film Coating, (1997), pp. 3–15.
- [29] M. KLEIN AND A. PROHL, *Optimal control for the thin film equation: Convergence of a multi-parameter approach to track state constraints avoiding degeneracies*, Computational Methods in Applied Mathematics, 16 (2016), pp. 685–702.
- [30] Y. LEE, H. THOMPSON, AND P. GASKELL, *Dynamics of thin film flow on flexible substrate*, Chemical Engineering and Processing: Process Intensification, 50 (2011), pp. 525–530.
- [31] Y. LOU AND P. D. CHRISTOFIDES, *Optimal actuator/sensor placement for nonlinear control of the kuramoto-sivashinsky equation*, IEEE Transactions on Control Systems Technology, 11 (2003), pp. 737–745.
- [32] D. LUNZ, *Minimizing deformation of a thin fluid film driven by fluxes of momentum and heat*, Physical Review E, 103 (2021), p. 033105.
- [33] A. MANZONI, A. QUARTERONI, AND S. SALSA, *Optimal control of partial differential equations*, Springer, 2021.
- [34] O. MATAR, R. CRASTER, AND S. KUMAR, *Falling films on flexible inclines*, Physical Review E, 76 (2007), p. 056301.
- [35] O. K. MATAR AND S. KUMAR, *Rupture of a surfactant-covered thin liquid film on a flexible wall*, SIAM Journal on Applied Mathematics, 64 (2004), pp. 2144–2166.
- [36] O. K. MATAR AND S. KUMAR, *Dynamics and stability of flow down a flexible incline*, Journal of Engineering Mathematics, 57 (2007), pp. 145–158.
- [37] C. MILES, K. G. V. D. ZEE, M. E. HUBBARD, AND R. MACKENZIE, *Thermomechanically-consistent phase-field modeling of thin film flows*, Numerical Methods for Flows: FEF 2017 Selected Contributions, (2020), pp. 121–129.
- [38] A. MIYARA, *Numerical analysis on flow dynamics and heat transfer of falling liquid films with interfacial waves*, Heat and Mass Transfer, 35 (1999), pp. 298–306.
- [39] A. ORON, S. H. DAVIS, AND S. G. BANKOFF, *Long-scale evolution of thin liquid films*, Reviews of modern physics, 69 (1997), p. 931.
- [40] O. REYNOLDS, *IV. on the theory of lubrication and its application to mr. beauchamp tower’s experiments, including an experimental determination of the viscosity of olive oil*, Philosophical transactions of the Royal Society of London, (1886), pp. 157–234.
- [41] M. SELLIER, *Substrate design or reconstruction from free surface data for thin film flows*, Physics of Fluids, 20 (2008).
- [42] M. SELLIER, *Inverse problems in free surface flows: a review*, Acta Mechanica, 227 (2016), pp. 913–935.
- [43] M. SELLIER AND S. PANDA, *Beating capillarity in thin film flows*, International

- journal for numerical methods in fluids, 63 (2010), pp. 431–448.
- [44] K. SERIFI, N. A. MALAMATARIS, AND V. BONTOZOGLOU, *Transient flow and heat transfer phenomena in inclined wavy films*, International journal of thermal sciences, 43 (2004), pp. 761–767.
 - [45] A. B. THOMPSON, S. N. GOMES, F. DENNER, M. C. DALLASTON, AND S. KALLIADASIS, *Robust low-dimensional modelling of falling liquid films subject to variable wall heating*, Journal of Fluid Mechanics, 877 (2019), p. 844–881, <https://doi.org/10.1017/jfm.2019.580>.
 - [46] A. B. THOMPSON, S. N. GOMES, G. A. PAVLIOTIS, AND D. T. PAPAGEORGIOU, *Stabilising falling liquid film flows using feedback control*, Physics of Fluids, 28 (2016), p. 012107.
 - [47] R. J. TOMLIN, R. CIMPEANU, AND D. T. PAPAGEORGIOU, *Instability and dripping of electrified liquid films flowing down inverted substrates*, Physical Review Fluids, 5 (2020), p. 013703.
 - [48] R. J. TOMLIN, S. N. GOMES, G. A. PAVLIOTIS, AND D. T. PAPAGEORGIOU, *Optimal control of thin liquid films and transverse mode effects*, SIAM Journal on Applied Dynamical Systems, 18 (2019), pp. 117–149.
 - [49] D. TSELUIKO, M. G. BLYTH, AND D. PAPAGEORGIOU, *Stability of film flow over inclined topography based on a long-wave nonlinear model*, Journal of Fluid Mechanics, 729 (2013), pp. 638–671.
 - [50] D. TSELUIKO AND D. T. PAPAGEORGIOU, *Wave evolution on electrified falling films*, Journal of Fluid Mechanics, 556 (2006), pp. 361–386.
 - [51] A. W. WRAY, R. CIMPEANU, AND S. N. GOMES, *Electrostatic control of the navier-stokes equations for thin films*, Physical Review Fluids, 7 (2022), p. L122001.
 - [52] X. WU, K. G. VAN DER ZEE, G. SIMSEK, AND E. VAN BRUMMELEN, *A posteriori error estimation and adaptivity for nonlinear parabolic equations using imex-galerkin discretization of primal and dual equations*, SIAM Journal on Scientific Computing, 40 (2018), pp. A3371–A3399.

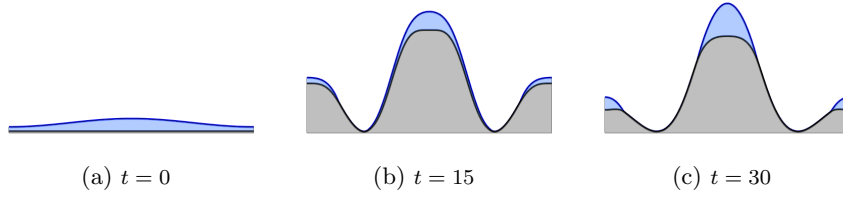


Fig. 18: Snapshots of the optimal solution, controlled towards a ruptured state. The solution is extended symmetrically in domain $[-L, L]$.

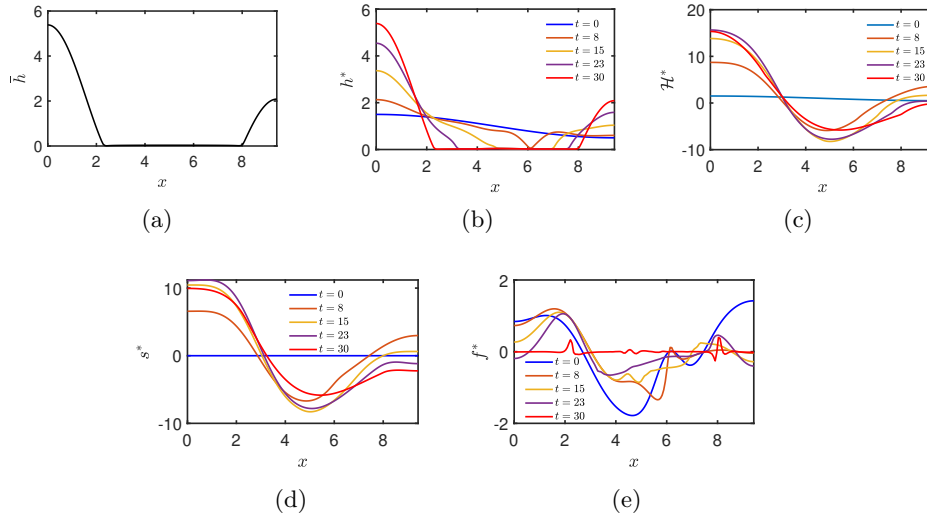


Fig. 19: (a) Target state \bar{h} . (b-e) Evolution of the optimal surface profile \mathcal{H}^* , film height h^* , topography s^* , and control f^* , respectively.

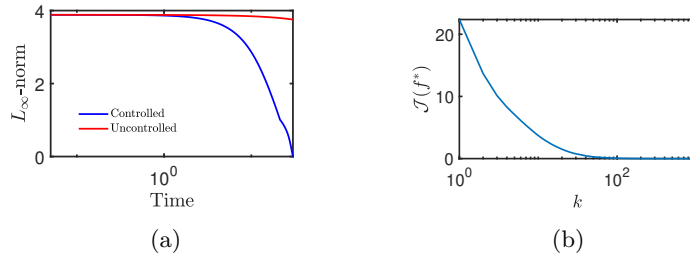


Fig. 20: (a) L^∞ -norm of the variation $h^* - \bar{h}_{\text{rupt}}$. (b) Cost function $\mathcal{J}(f^*)$ against number of iterations k .

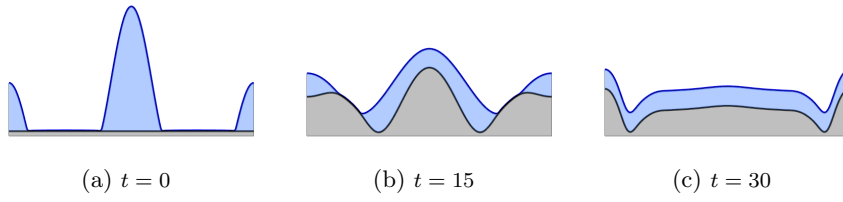


Fig. 21: Snapshots of the optimal solution, controlled from a ruptured state to a uniform film thickness. The solution is extended symmetrically in domain $[-L, L]$.

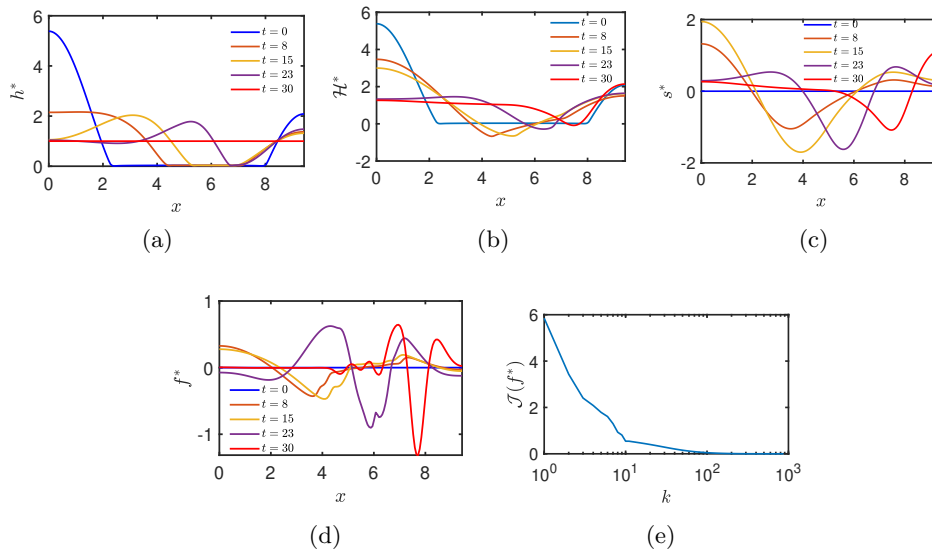


Fig. 22: (a-d) Evolution of the optimal surface profile \mathcal{H}^* , film height h^* , topography s^* , and control f^* , respectively. (e) Cost function $\mathcal{J}(f^*)$ against number of iterations k .